crystals MDPI

Article

X-ray Diffraction, Spectroscopy, Optical Properties, NPA, NBO, FMO, and Hirshfeld Surface Analyses of Two Newly Synthesized Piperidinium Ionic Liquids

Youness El Bakri [1,*], Shaaban K. Mohamed [2,*], Atazaz Ahsin [3], Etify A. Bakhite [4], Islam S. Marae [4], Safiyyah A. H. Al-waleedy [4], Joel T. Mague [5] and Rashad Al-Salahi [6]

[1] Department of Theoretical and Applied Chemistry, South Ural State University, Lenin Prospect 76, Chelyabinsk 454080, Russia
[2] Chemistry and Environmental Division, Manchester Metropolitan University, Manchester M1 5GD, UK
[3] Beijing National Laboratory for Molecular Sciences, Institute of Chemistry, Chinese Academy of Sciences, Beijing 100190, China; ahsin@iccas.ac.cn
[4] Chemistry Department, Faculty of Science, Assiut University, Assiut 71516, Egypt; betiafy@yahoo.com (E.A.B.); esllamsalem@aun.edu.eg (I.S.M.)
[5] Department of Chemistry, Tulane University, New Orleans, LA 70118, USA; joelt@tulane.edu
[6] Department of Pharmaceutical Chemistry, College of Pharmacy, King Saud University, Riyadh 11451, Saudi Arabia; ralsalahi@ksu.edu.sa
* Correspondence: yns.elbakri@gmail.com (Y.E.B.); shaabankamel@yahoo.com (S.K.M.)

Abstract: The present study elaborates on the synthesis, crystal structure, and computational studies of two new ionic liquids. In the crystal structure, $[C_5H_{12}N][C_{21}H_{14}ClN_2O_2S]$ (**4a**), the anions form chains along the *a*-axis direction through C—H···π(ring) interactions. These are connected into layers that run approximately parallel to the *ac* plane by a variety of hydrogen bonds. In the compound structure, $[C_5H_{12}N][C_{18}H_{15}N_2O_2S]$ (**4b**), the two ions are primarily associated by an N—H···N hydrogen bond. In the crystal structure, layers parallel to the *bc* plane are formed by pairs of C—H···O and N—H···S hydrogen bonds and by C—H···π(ring) interactions. A theoretical study reveals that **4a** has lower energy than **4b** and is more stable. The NBO and DOS studies further confine the liquids' structural reactivity and electronic properties. The quantum theory of atoms in a molecule (QTAIM) analysis reveals the important non-covalent interactions among the fragments and charge transfer. The global reactivity descriptors indicate their molecular reactivity relationship with the presence of functional groups. The remarkable polarizability (α_o) and hyperpolarizability (β_o) values indicate their optical and nonlinear optical (NLO) properties. Furthermore, the analysis performed by CrystalExplorer shows the intermolecular interactions and reactive sites between cations and anions in ionic liquids. The 2D fingerprint plots and Hirshfeld surfaces indicate the major interactions of crystals with neighboring elements in crystal packing. For both compounds, the H···H interactions are significantly higher than the other element interactions.

Keywords: ionic liquids; single crystal X-ray diffraction crystallography; FMO; NBO; NLO properties

check for updates

Citation: El Bakri, Y.; Mohamed, S.K.; Ahsin, A.; Bakhite, E.A.; Marae, I.S.; A. H. Al-waleedy, S.; Mague, J.T.; Al-Salahi, R. X-ray Diffraction, Spectroscopy, Optical Properties, NPA, NBO, FMO, and Hirshfeld Surface Analyses of Two Newly Synthesized Piperidinium Ionic Liquids. *Crystals* **2023**, *13*, 1583. https://doi.org/10.3390/cryst13111583

Academic Editor: Benoit Heinrich

Received: 24 September 2023
Revised: 2 November 2023
Accepted: 9 November 2023
Published: 14 November 2023

1. Introduction

Given the abundance of pyridine and its derivatives in nature and the significance of niacin for the treatment of dementia and dermatitis, pyridine and its targets became intriguing in 1930 [1]. Functionally substituted pyridines are bioactive small molecules that possess a wide range of biological activities and therapeutic uses [2–4], and many of them are now used in clinical settings [5]. For example, Actos, which is a drug that is widely used as an anti-diabetic agent, and vitamins such as B6 which play key roles in metabolism are pyridine-based structures [6,7]. In particular, it was discovered that substituted cyanopyridines have antipyretic, anti-inflammatory, and analgesic properties [8] as well as antihypertensive [9], antimicrobial [10], cardiotonic [11], and anticancer activities [12,13]. Among the successful examples of drug candidates possessing the pyridine core are streptonigrone, lavendamycin, and streptonigrin, which are depicted in the literature as anticancer agents [14].

Moreover, thieno-pyridine derivatives have been included in several medicinal preparations including antiviral [15], antihypertensive [16], antimicrobial [17], and anti-inflammatory [18] agents. In addition, pyrimidines act as antipyretic [19,20], antimicrobial [21], antiallergic [22,23], anti-anaphylactic [24,25], anticancer [26–28], and antiprotozoal agents [29].

On other hand, the literature showed that ionic liquids in general play an important role in industrial and biological applications [30]. Ionic liquids are considered as good molecular solvents compared to the commonly used volatile organic solvents [31]. They also could serve as clean and green solvents in pharmaceutical industries due to their broad range of polarities and their combinations of cations (particularly organic) and anions which could ease the solubility of an extensive range of drugs [32]. They also possess a very low viscosity, low vapor pressure or non-volatility under ambient conditions, tuneable solubility, acidity, basicity, long range thermal stability, and very low corrosivity relative to mineral acids and bases, etc. [33]. They also have no side effects on atmospheric photochemistry [34]. Moreover, the non-volatile nature of most ionic liquids also causes them to be non-flammable under ambient conditions, which includes low-boiling solvents such as petroleum ether, dichloromethane, acetone, and many more [35]. Because of their unique properties, the synthesis of ionic liquids becomes so important for various interests such as electro-chemists, analysts, biologists, engineers, physical chemists, and many more types of chemists. However, their synthesis and purification require standard synthesis methods to certify their consistent reproducibility. Piperidinium-based ionic liquids in particular have been used as effective catalysts in biomass conversion [36].

With these facts in mind, we decided to study two piperidinum ionic liquid derivatives of cyanopyridine thiones.

DFT-based investigations play a vital role in determining the reactivity and structural properties of new compounds. Non-covalent interactions, charge transfer, and π-conjugation have made organic molecules interesting moieties for studying electronic and optical properties. In our current study, we have employed DFT and Hirshfeld analyses to understand the structural reactivity and crystal properties of our liquid crystals, in particular their nonlinear optical (NLO) properties.

2. Experimental

2.1. Materials and Methods

All the chemicals and solvents used in the synthesis and spectroscopic experiments are commercially available and utilized as such. The melting points were determined using a Gallenkamp instrument (Assiut University, Assiiut, Egypt) and are uncorrected. A PerkinElmer 2400 LS Series CHN/O analyzer was used for elemental analyses (C, H, and N) (Universiti Sains 48 Malaysia, Minden, Malaysia). Ethyl 3-oxobutanoate (**1a**), ethyl 3-oxo-3-phenylpropanoate (**1b**), and the appropriate used aldehydes and solvents were purchased from Sigma-Aldrich chemicals. The arylidines (**2a**,**b**) had been prepared in our lab by refluxing the appropriate aldehyde with the corresponding 2-cyanoethanethioamide in ethanol for the interval time.

The reactions in this study were monitored with TLC (thin-layer chromatography) on Merck alumina-backed TLC plates Pf254 using UV light. FTIR spectra were collected with a Pye-Unicam SP3-100 spectrophotometer using the KBr disc technique (ν_{max}, in cm^{-1}) (Assiut University, Assiut, Egypt). NMR spectra were measured on a Bruker spectrometer (at 400 MHz for ^{1}H NMR and 101 MHz for ^{13}C NMR) in $CDCl_3$ solutions (except for **2b**, which was in DMSO-d$_6$), with chemical shifts reported in (ppm) and coupling constants (*J* values) given in Hz (Sohag University, Sohag, Egypt).

2.2. Synthesis

2.2.1. Synthesis of Piperidinium [4-(4-chlorophenyl)-3-cyano-5-(ethoxycarbonyl)-6-phenylpyridin-2-yl]sulfanide (Scheme 1; **4a**)

A mixture of 4-(4-chlorophenyl)-3-cyano-5-ethoxcarbonyl-6-phenylpyridine-2(1*H*)-thione, **3a**, (10 mmol) and piperidine (15 mmol) in ethanol (35 mL) was heated under reflux for 15 min and then allowed to cool. The crystalline solid that formed was collected using filtration, air-dried, and recrystallized from ethanol to give one spot product on the TLC plate under UV light (99.9% purity) orange needles of **4a**; Yield: 80%. m. p. 219–221 °C. FTIR (ν) (KBr), cm^{-1}: 3420, 2480, 2400 (N^+H_2), 2952 (C-H, aliphatic), 2215 (C≡N), 1726 (C=O). ^{1}H NMR ($CDCl_3$): δ 7.20–7.33 (m, 11H, N^+H_2 and Ar-H), 3.70–3.71 (q, 2H, OCH_2), 2.86 (t, 4H, $CH_2N^+CH_2$), 1.35–1.37 (m, 4H, $2CH_2$), 1.18 (m, 2H, CH_2), 0.69 (t, 3H, CH_3). Anal. Calcd. for $C_{26}H_{26}ClN_3O_2S$ (%): C, 65.06; H, 5.46; N, 8.75; S, 6.68. Found (%): C, 64.78; H, 5.22; N, 8.51; S, 6.92.

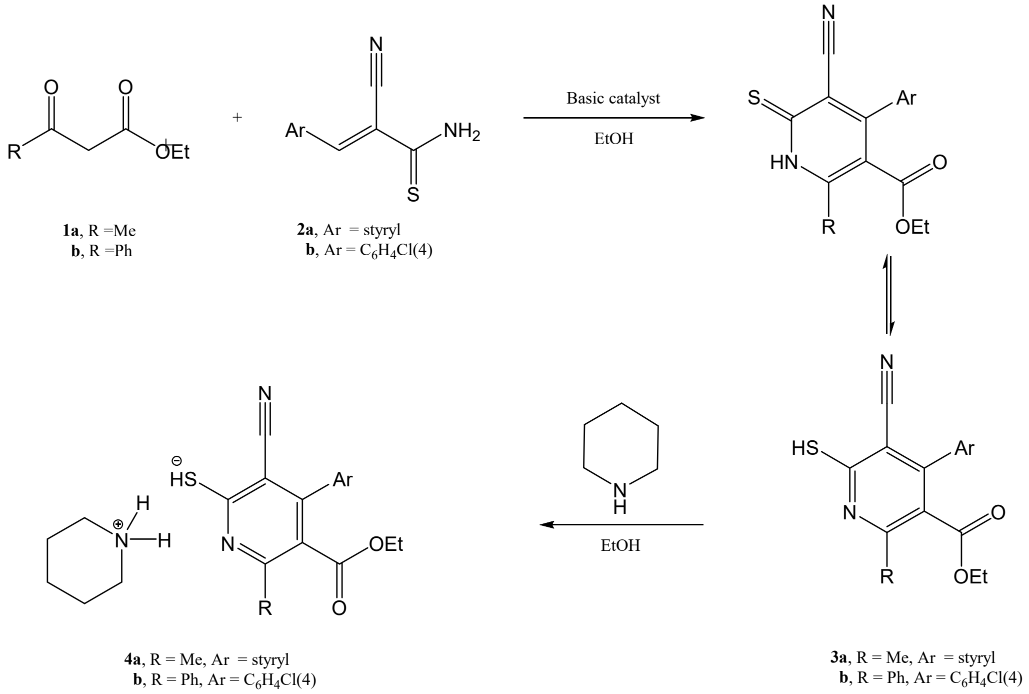

Scheme 1. Synthesis of (**4a**,**b**).

2.2.2. Synthesis of Piperidinium [3-cyano-5-(ethoxycarbonyl)-6-methyl-4-[(E)-2-phenylethenyl]pyridin-2-yl]sulfanide (Scheme 1; **4b**)

A mixture of 3-cyano-5-ethoxcarbonyl-6-methyl-4-styryl-pyridine-2(1*H*)-thione, **3b**, (3.24 g, 10 mmol) and piperidine (10 mmol) in ethanol (25 mL) was heated under reflux for 15 min and then allowed to cool. The crystalline solid that formed was collected using filtration, air-dried, and recrystallized from ethanol to give absolute pure spot in TLC plate under UV light (100% purity) yellow needles of **4b**; yield: 3.76 g (92 %); m.p: 241–243 °C. Its FTIR spectrum showed characteristic absorption bands at 3430, 2508, 2410 cm^{-1} for (N^+H_2), 2948, 2755 cm^{-1} for (C-H, aliphatic), 2211 cm^{-1} for (C≡N), and 1728 cm^{-1} for (C=O) (see the supplementary materials). Its ^{1}H NMR spectrum ($CDCl_3$) displayed a broad singlet at δ 8.61 (2H, NH_2), a multiplet at δ 7.10–7.49 (m, 7H: CH=CH and Ar-H's), a quartet at δ 4.27–4.32 (2H, OCH_2), a triplet at δ 3.23–3.25 (4H, CH_2NCH_2), a singlet at δ 2.41 (3H, CH_3), a pentet at δ 1.81–1.86 (4H, CH_2-C-CH_2), a triplet at δ 1.64–1.66 (2H, C-C-CH_2-C-C), and a triplet at δ 1.25–1.28 (3H, CH_3 of ester group) ppm (see the supplementary materials). Its ^{13}C NMR spectrum ($CDCl_3$) showed the following peaks: δ 180.30, 168.42, 156.37, 147.17, 137.99, 135.91, 129.08, 128.77, 127.19, 122.64, 119.33, 119.29, 108.30, 61.59, 44.87, 23.35, 23.02, 22.52, and 14.16 ppm. Anal. Calcd. for $C_{23}H_{27}N_3O_2S$ (409.09): C, 67.45; H, 6.65; N, 10.26; S, 7.83%. Found: C, 67.20; H, 6.61; N, 10.51; S, 7.54% (see the supplementary materials).

2.3. Crystal Structure Measurement

Suitable crystals of **3a** and **3b** were put on polymer loops with a drop of heavy oil and placed in a stream of cold nitrogen on a Bruker Smart APEX CCD diffractometer (Bruker AXS Inc., Madison, Wisconsin, USA) equipped with a fine-focus sealed tube (Mo$K\alpha$, $\lambda = 0.71073$ Å) and a graphite monochromator. The APEX3 software [37] was used to collect the intensity data, and SAINT [37] was used to convert the raw intensities to F^2 values. SADABS [38] was used to apply numerical absorption corrections and merge the equivalent reflections. The structures were solved using dual space methods (SHELXT [38]) and refined by full-matrix, least-squares methods (SHELXL [39]). All hydrogen atoms were located in different maps and were refined independently except for those attached to C18 in **4b**, which were included as riding contributions in idealized positions. For **4a**, the C alert is the result of some minor disorder of that methyl group which causes an apparent large displacement parameter. The disorder, however, is not large enough to be refined with a split-atom model. For **4b**, although the ratio of Maximum/Minimum Residual Density is 2.19, the actual values are 0.490 and −0.224 e-Å–3, which are no more than half a hydrogen atom and so are not considered significant. The Hirshfeld test on the S1—C1 bond is likely due to S1 being a terminal atom and relatively unconstrained in its vibrational motion along the S1—C1 bond, while C1 is part of the six-membered ring and so is much more constrained in its vibrational motions. The “missing reflections” (only four) are inaccessible with the diffractometer used or are obscured by either the beam stop or the nozzle of the low-temperature unit. Table 1 provides crystallographic details.

Table 1. Crystal and refinement details for **4a** and **4b**.

Compound	**4a**	**4b**
CCDC Deposit Number	2237196	2237198
Chemical formula	$C_{21}H_{14}ClN_2O_2S{\cdot}C_5H_{12}N$	$C_{18}H_{15}N_2O_2S{\cdot}C_5H_{12}N$
M_r	480.01	409.53
Crystal system, space group	Monoclinic, $P2_1/c$	Triclinic, $P\overline{1}$
Temperature (K)	120	120
a, b, c (Å)	7.6105 (4), 26.1975 (14), 12.2488 (7)	10.0768 (4), 10.4188 (4), 11.3759 (5)
α, β, γ (°)	β (°) = 99.357 (1)	78.519 (1), 82.891 (1), 65.707 (1)
V (Å^3)	2409.6 (2)	1065.63 (8)
Z	4	2
Radiation type	Mo $K\alpha$	Mo $K\alpha$
μ (mm^{-1})	0.27	0.18
Crystal size (mm)	0.21 × 0.20 × 0.09	0.30 × 0.27 × 0.17
	Data collection	
Diffractometer	Bruker Smart *APEX* CCD	Bruker Smart *APEX* CCD
T_{min}, T_{max}	0.92, 0.97	0.82, 0.90
No. of measured, independent and observed [$I > 2\sigma(I)$] reflections	22901, 6129, 4967	20787, 5673, 4716
R_{int}	0.028	0.025
$(\sin\theta/\lambda)_{max}$ (Å^{-1})	0.685	0.686
	Refinement	
$R[F^2 > 2\sigma(F^2)]$, $wR(F^2)$, S	0.037, 0.105, 1.09	0.039, 0.115, 1.11

Table 1. *Cont.*

Compound	4a	4b
No. of reflections	6129	5673
No. of parameters	391	370
H-atom treatment	All H-atom parameters refined	H atoms treated by a mixture of independent and constrained refinement
$\Delta\rho_{max}$, $\Delta\rho_{min}$ (e Å^{-3})	0.42, −0.22	0.49, −0.22

2.4. Computational Details

The applicability of the density functional theory (DFT) for defining and understanding crucial chemical ideas of molecular structure and reactivity is one of its most relevant features [40]. Here, density functional theory (DFT) is used to theoretically investigate **4a** and **4b** using the Gaussian 09 program [41] with GaussView 5.0 being used to display the resulting geometries [42]. All calculations were run at the B3LYP functional level using the split valence double zeta basis set 6-31+G(d,p). For organic molecules, the B3LYP method is reliable for determining long-range, non-covalent interactions and has a hybrid function. After the geometries were optimized, frequency calculations were performed to ensure the stability of the resulting structures. Additionally, we calculated the ionization potential and electron affinity of **4a** and **4b** to assess their electronic stability and reactivity and used frontier molecular orbital theory (FMOs) and NBO charge analysis to obtain more specific details.

To determine the conductivity and reactivity of the compounds, we conducted density of states (DOS) studies and estimated their optical and nonlinear optical characteristics using the same theoretical approach which provided values for the dipole moments (μ_o), polarizability (α_o), hyperpolarizability (β_o), and the projection of the hyperpolarizability on the dipole moment vector. Additionally, we performed 3D Hirshfeld surface analyses, including fingerprint plots of **4a** and **4b**, to visualize intermolecular interactions in the crystals using CrystalExplorer 21.5 [43].

3. Results and Discussion

3.1. X-ray Diffraction Studies

3.1.1. Crystal Structure of 4a

The phenyl and 4-chlorophenyl rings are inclined to the central pyridine ring by 49.98(4)° and 62.34(4)°, respectively (Figure 1). In the crystal, the anions form chains extending along the *a*-axis direction through inversion-related C13—H13A··· Cg2 interactions (Table 2 and Figure 2) between the ethoxycarbonyl substituents and the phenyl substituents on neighboring units. These are constructed into layers that are approximately parallel to the *ac* plane and two anions thick by intervening sets of cations through N3—H3A···S1 and N3—H3B···S1 hydrogen bonds assisted by C25—H25A···O2, C25—H25B···S1, C19—H19···O1 and C22—H22B···N2 hydrogen bonds (Table 2 and Figures 2 and 3).

Table 2. Hydrogen-bond geometry (Å,°) in **4a**.

D—H···*A*	*D*—H	H···*A*	*D*···*A*	*D*—H···*A*
N3—H3A···S1^{i}	0.875(19)	2.486(19)	3.3011(12)	155.3(16)
N3—H3B···S1^{ii}	0.953(18)	2.406(18)	3.2504(12)	147.6(14)
C13—H13A···Cg2^{i}	1.01(2)	2.87(2)	3.6702(17)	136.0(14)
C19—H19···O1^{iii}	0.934(17)	2.552(17)	3.2713(17)	134.2(13)
C22—H22B···N2^{i}	1.000(17)	2.597(17)	3.3280(19)	129.8(12)
C25—H25A···O2^{iv}	0.983(18)	2.518(18)	3.2771(18)	133.9(13)
C25—H25B···S1^{i}	0.954(17)	2.870(18)	3.6474(16)	139.4(13)

Symmetry codes: (i) x + 1, y, z; (ii) x + 1, −y + 1/2, z−1/2; (iii) −x + 1, −y + 1, −z + 1; (iv) x, −y + 1/2, z − 1/2. Cg2 is the centroid of the C6···C11 benzene ring.

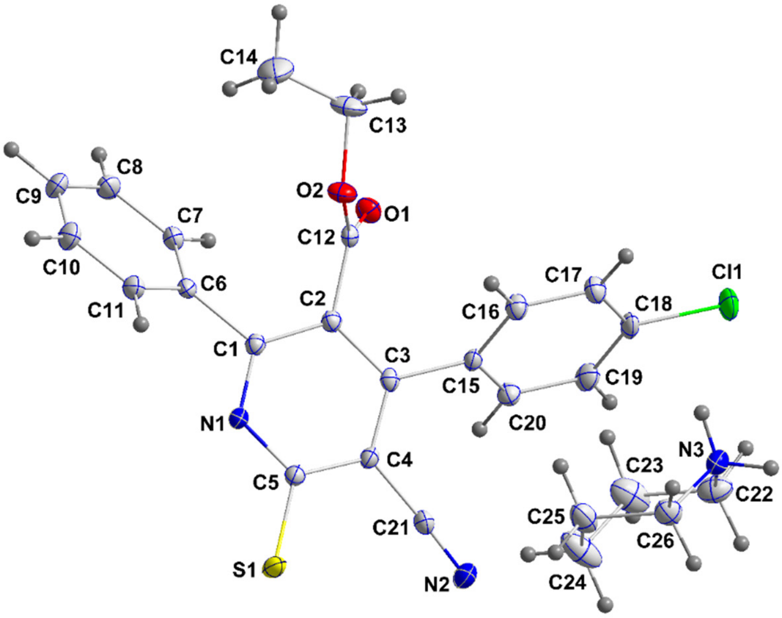

Figure 1. Perspective view of **4a** with the labeling scheme and 50% probability ellipsoids.

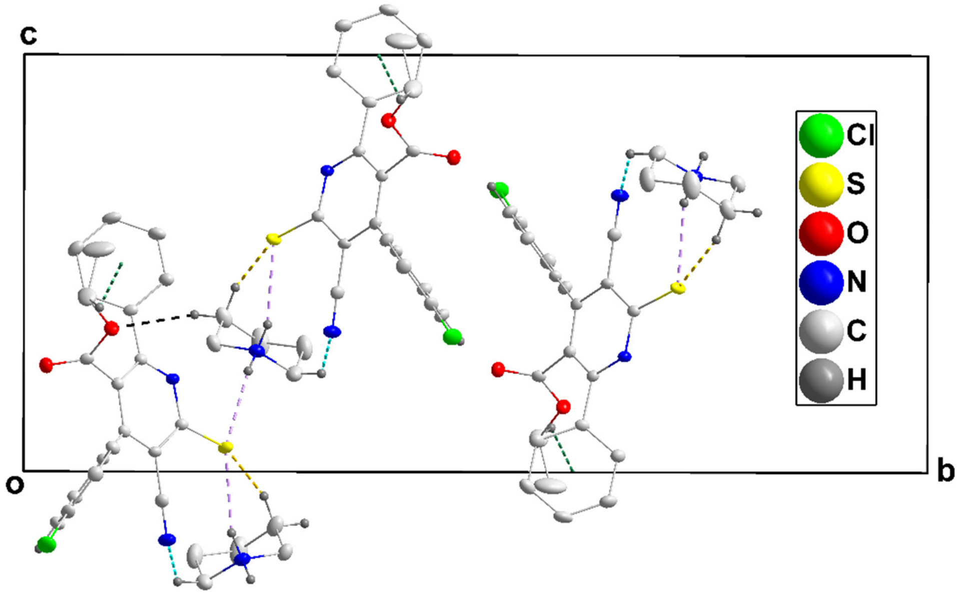

Figure 2. End view of portions of the two layers seen along the *a*-axis direction. N—H···S, C—H···O, C—H···N, and C—H···S hydrogen bonds are shown, respectively, by light violet, black, light blue, and gold dashed lines. The C—H···π(ring) interactions are shown by green dashed lines.

3.1.2. Crystal Structure of **4b**

The dihedral angle between the N1/C1···C5 and C9···C14 rings is 48.62(5)°, while the piperidinium cation adopts a chair conformation (Figure 4). In the crystal, two formula units form inversion dimers through N3—H3B···N1 and N3—H3A···S1 hydrogen bonds (Table 3 and Figure 5). The dimers are connected into zigzag chains extending along the *c*-axis direction by inversion-related C19—H19B···O1 and C23—H23B···O1 hydrogen bonds as well as C21—H21B···Cg2 interactions (Table 3 and Figure 5). Finally, the chains are connected into layers that are parallel to the *bc* plane by inversion-related C14—H14···Cg1 interactions (Table 3 and Figures 5 and 6).

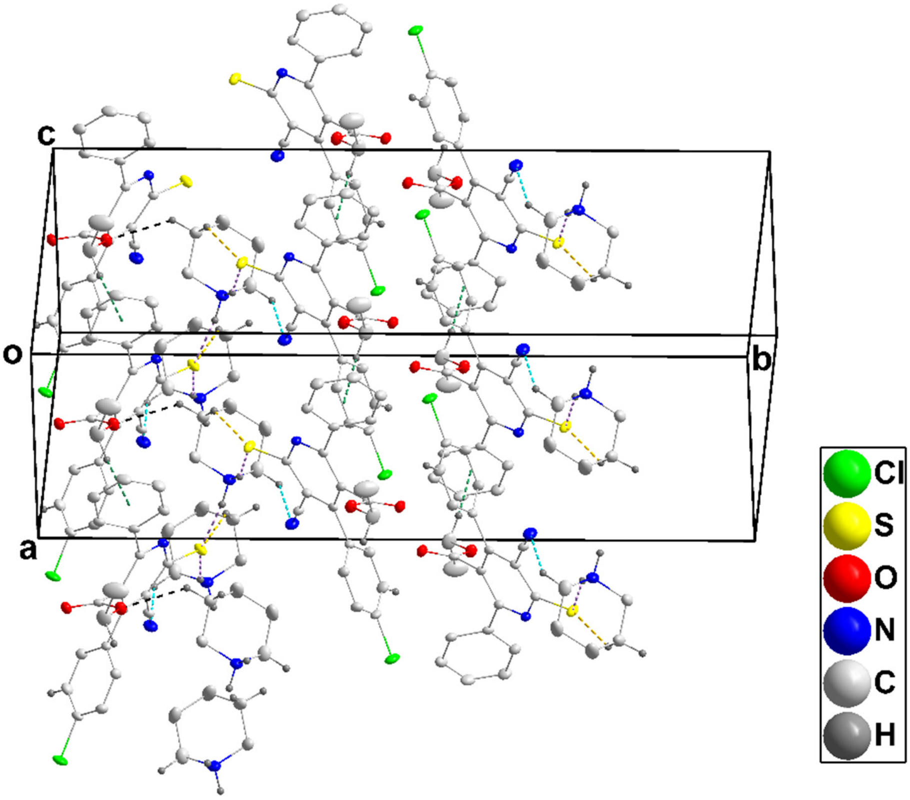

Figure 3. Details of the interionic interactions in **4a**. N—H···S, C—H···O, C—H···N and C—H···S hydrogen bonds are shown, respectively, by light violet, black, light blue, and gold dashed lines. The C—H···π(ring) interactions are shown by green dashed lines.

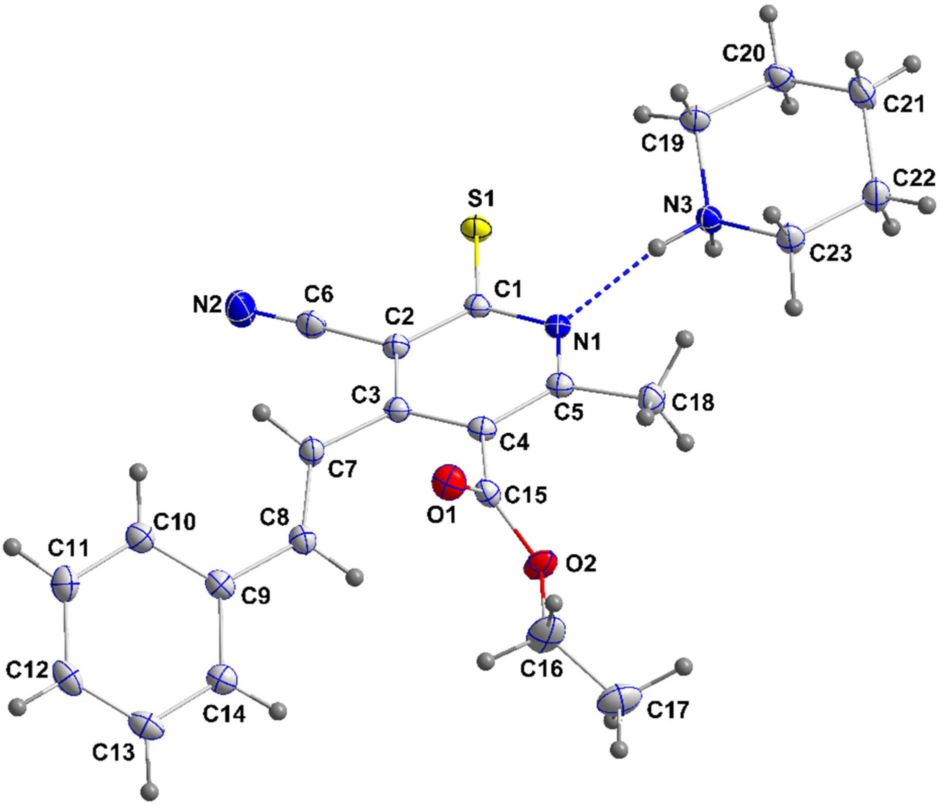

Figure 4. Perspective view of **4b** with the labeling scheme and 50% probability ellipsoids. The interionic hydrogen bond is shown by a dashed line.

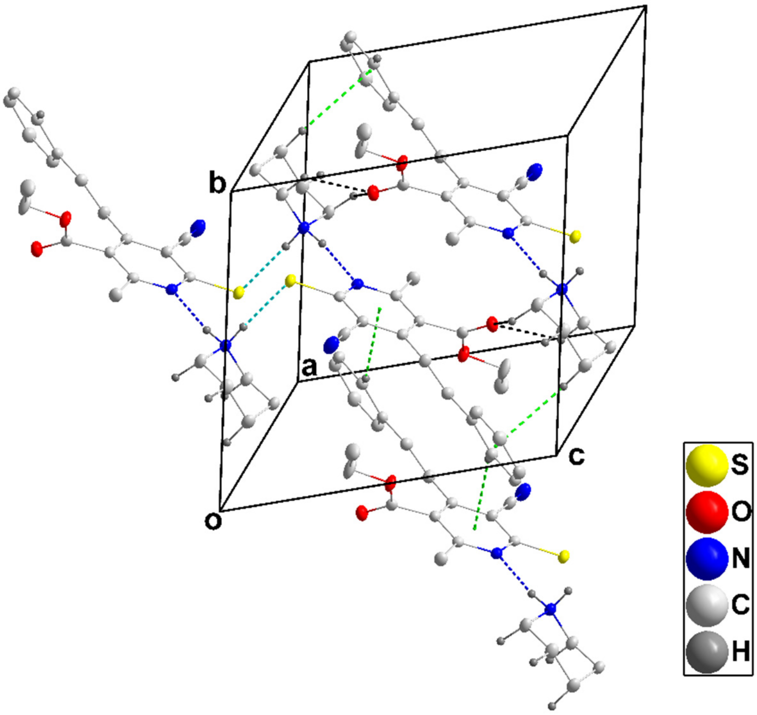

Figure 5. Details of the interionic interactions in **4b**. N—H···N, C—H···O, and N—H···S hydrogen bonds are depicted, respectively, by dark blue, black, and light blue dashed lines. The C—H···π(ring) interactions are shown by green dashed lines.

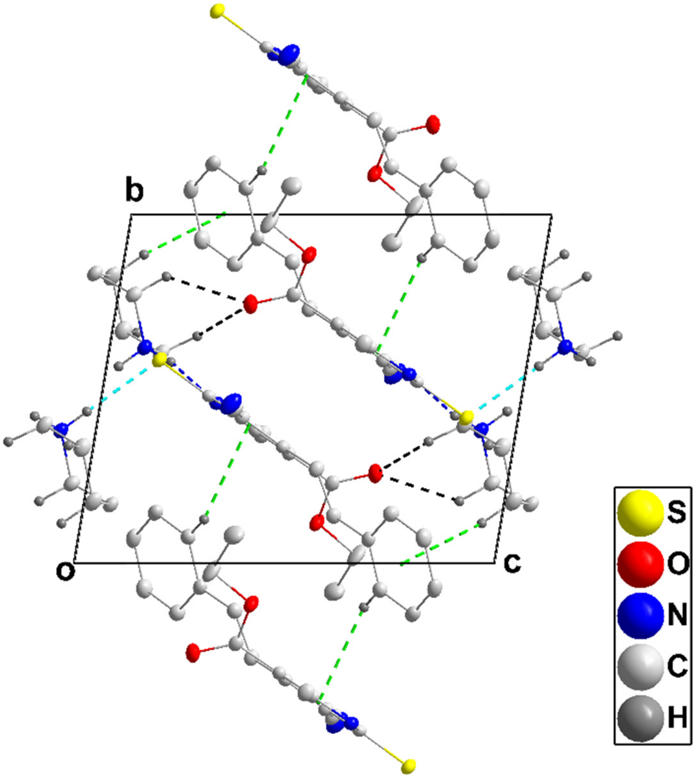

Figure 6. Packing in **4b** viewed along the *a*-axis direction with interionic interactions as shown in Figure 5.

Table 3. Hydrogen-bond geometry (Å,°) for **4b**.

D*—H···*A	***D*—H**	**H···*A***	***D*···*A***	***D*—H···*A***
N3—H3A···S1^{i}	0.883(15)	2.393(15)	3.2702(10)	172.1(12)
N3—H3B···N1	0.980(16)	1.980(17)	2.9479(12)	169.0(14)
C14—H14···Cg1^{ii}	0.971(16)	2.848(15)	3.6112(13)	136.2(13)
C19—H19B···O1^{iii}	1.001(15)	2.387(15)	3.1508(14)	132.4(11)
C21—H21B···Cg2^{iii}	0.948(16)	2.972(16)	3.9189(14)	151.4(13)
C23—H23B···O1^{iii}	1.068(14)	2.592(14)	3.3617(14)	128.4(10)

Symmetry codes: (i) −x + 1, −y + 1, −z; (ii) −x + 1, −y, −z + 1; (iii) −x + 1, −y + 1, −z + 1. Cg1 and Cg2 are, respectively, the centroids of the N1/C1···C5 and C9···C14 rings.

3.2. Optimized Geometries and Stability of Ionic Liquids

The optimized geometries of ionic liquids (**4a** and **4b**) are given in Figure 7. Initially, we obtained the geometries at the B3LYP/6-31+g(d,p) functional without any geometry constraints. The compounds have *C1* point group symmetry with non-planar geometries. The geometries obtained are real minima on the potential energy surface and have no negative (imaginary) frequencies associated with them. Thus, the structures are said to be stable with **4a** having a total electronic energy of −2179.57 Hartree, while −1605.68 Hartree is calculated for 4b, showing that **4a** is more stable than **4b** (Table 4)**.** For **4a**, the dipole moment μ_o was calculated to be 22.92 Debye, but for **4b**, it was only 9.46 Debye. The high dipole moment for **4a** can be attributed to the large charge separation within it, which is possibly due to the presence of the electronegative Cl-atom in the *para*-position. The asymmetric charge distribution and non-zero dipole moments exhibit intriguing electronic features and can be examined further for optical properties.

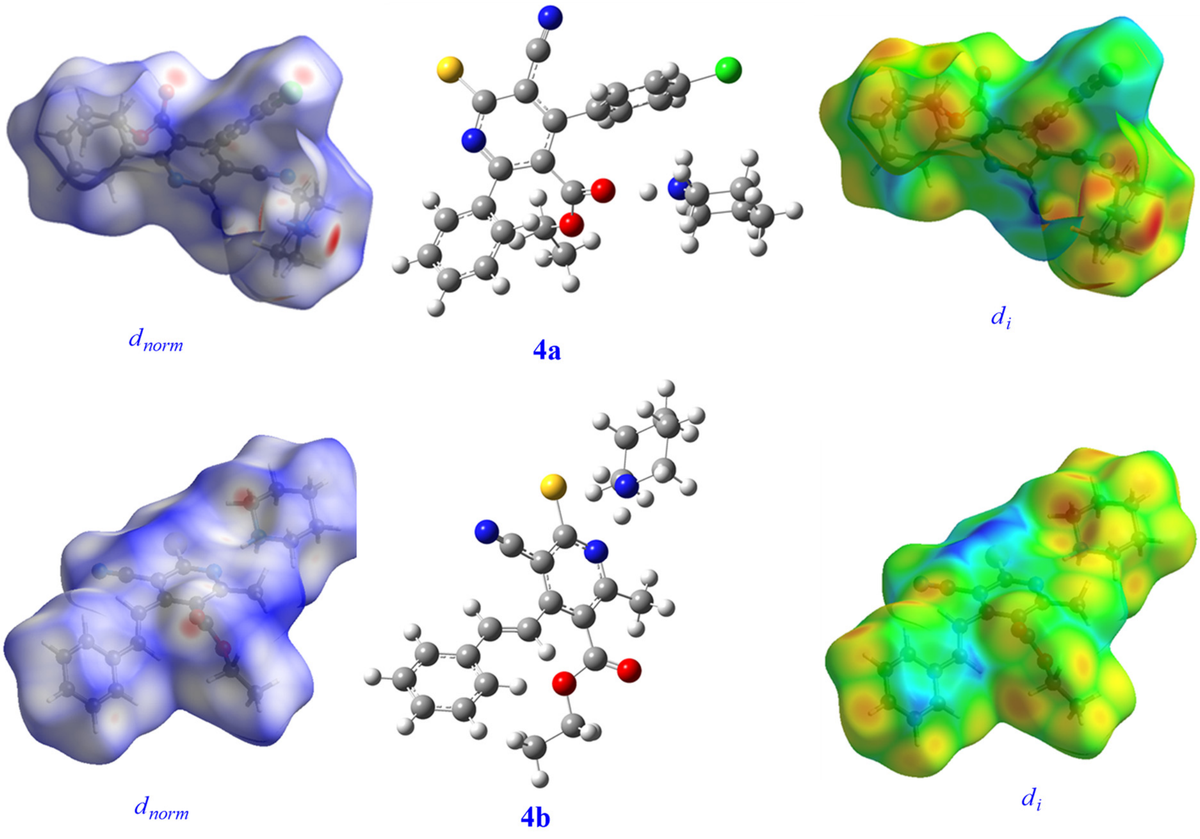

Figure 7. Optimized geometries at the B3LYP level and d_{norm} and d_i images of **4a** and **4b**.

Table 4. Point group symmetry, total electronic energy (in Hartree), mean dipole moment (μ_o in au), polarizability (α_o in au), average polarizability volume (α_v in Å^3), hyperpolarizability (β_o in au), and vector part of hyperpolarizability (β_{vec} in au) of **4a** and **4b**.

Parameters	**4a**	**4b**
Symmetry	C_1	C_1
Total energy	−2179.57	−1605.68
Dipole moment	22.923	9.46
Polarizability (α_o)	402.47	368.105
Isotropic average polarizability volume	59.64	54.547
Hyperpolarizability (β_o)	2400.72	2722.63
β_{vec}	2382.71	2660.48

3.3. FMOS Analysis and NBO Charge Study

To examine the reactivity and kinetic stability of organic compounds, frontier molecular orbital (FMO) analysis is a vital quantum chemical tool. Additionally, FMO theory plays a vital role in the interpretation of stereo- and regioselectivities of compounds. The lowest unoccupied molecular orbital (LUMO) and the highest occupied molecular orbital (HOMO) are included in the FMOs, as well as their band gaps ($E_{H\text{-}L}$). The calculated values of HOMO, LUMO, and their HOMO-LUMO gaps ($E_{H\text{-}L}$) are given in Table 5, and the pictorial representation of the HOMO and LUMO densities is shown in Figure 8. The calculated HOMO energy values are −4.51 and −5.35 eV for **4a** and **4b**, respectively, with HOMO-LUMO gaps of 2.78 and 3.39 eV, respectively. The relatively low $E_{H\text{-}L}$ gaps indicate the reactivity toward incoming moieties and the soft nature of **4a** and **4b**. The plotted densities of occupied and virtual orbitals are given in Figure 8.

Table 5. Energies of HOMO and LUMO (in eV), HOMO-LUMO gaps ($E_{H\text{-}L}$ in eV), NBO charges (QX in eV), ionization potential (IP in eV), electron affinity (EA in eV), chemical hardness (η in eV), chemical potential (μ in eV), electronegativity (χ in eV), and electrophilicity index (ω in eV) for **4a** and **4b**.

Parameters	**4a**	**4b**
E_{HOMO}	−4.511	−5.35
E_{LUMO}	−1.72	−1.95
$E_{H\text{-}L}$	2.78	3.39
Q(N/O/S)	−0.67/−0.71/−0.15	−0.72/−0.61/−0.274
Q(Cl)	−0.002	–
Ionization potential (IP)	4.51	5.35
Electron affinity (EA)	1.72	1.95
Chemical hardness (η)	1.39	1.71
Chemical potential (μ)	−3.11	−3.65
Electronegativity (χ)	3.11	3.65
Electrophilicity index (ω)	3.47	3.89

The natural bonding molecular orbital (NBO) charges for **4a** on nitrogen Q(N), oxygen Q(O), and sulfur Q(S) are −0.67, −0.71, and −0.15 |e|, respectively (Table 5). The highest NBO charge (negative) is found for carbon attached to oxygen in the central ring. The more negative charge indicates that the oxygen atom pulls the electrons to its p-orbitals from the carbon atom due to its high electronegativity. All the oxygen and nitrogen atoms have negative NBO charges, indicating their donor abilities in ionic liquid crystals. In **4a**, the cationic part ($C_5H_{12}N$) interacts through the oxygen atom of the anionic part of the compound. There is a more significant charge transfer (+0.50) from the hydrogen of cation to the oxygen of anion than those of **4b.** The anionic oxygen atom acts as a donor and has a significant negative NBO charge (−0.71 |e|). In **4b**, the hydrogen atom (attached to the cation) gets less partial positive charge (+0.42) after its interaction with the nitrogen of the anionic part. In **4b**, the nitrogen atom of the anionic part also bears less partial negative charge as compared to **4a**. Also, the N and S atoms' decreased NBO (negative) charges match their reduced electronegativity as compared with oxygen. Likewise, compound **4b** has the highest negative charge, up to −0.72, as can be seen on the nitrogen of the cationic part, while the charge on Sulphur Q(N) is −0.27 |e|. The entire hydrogen atoms attached to carbon atoms of **4a** and **4b** show positive NBO charges which indicate the transfer of charge from the s-orbital of hydrogen to p-of carbon-atom.

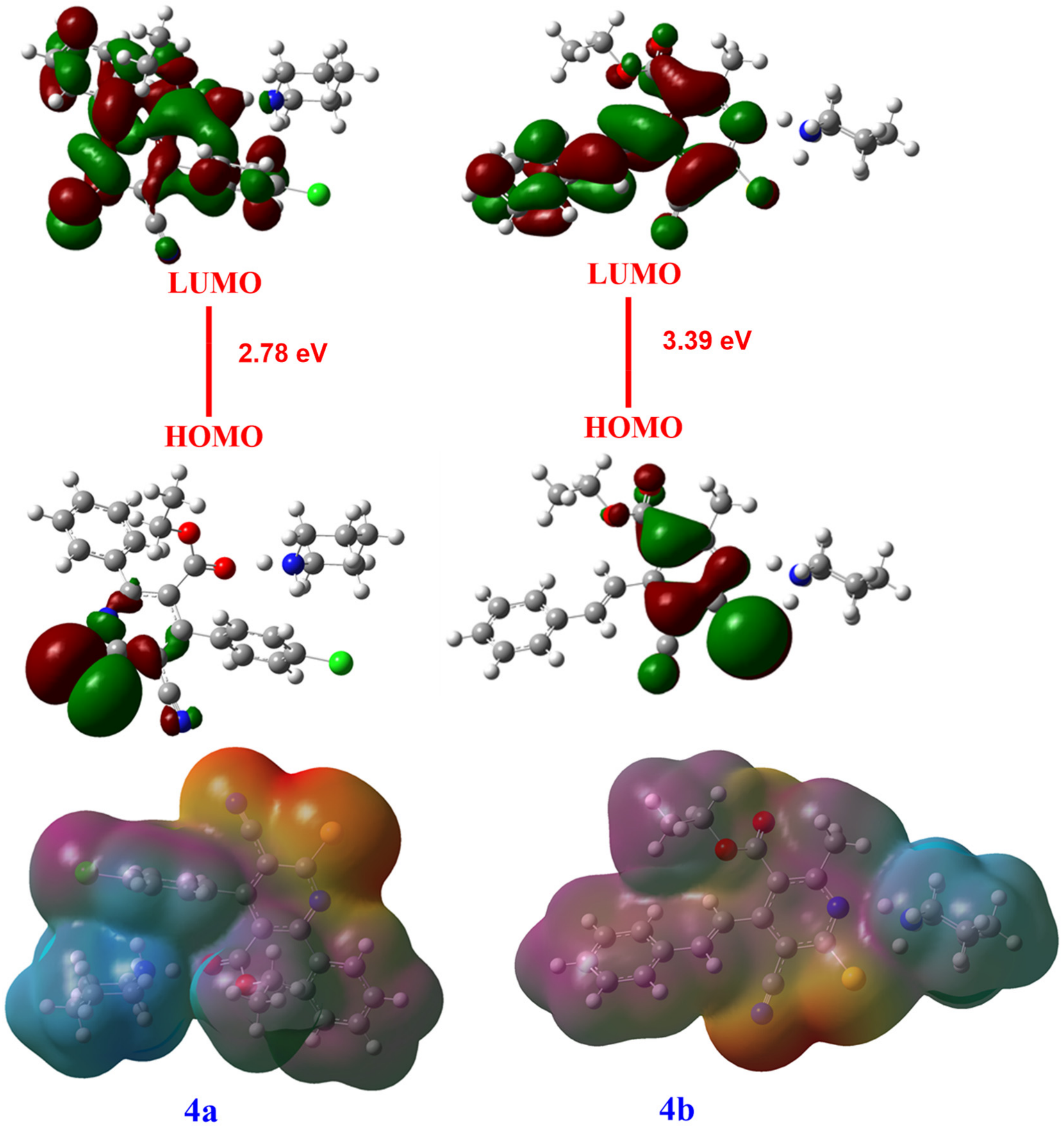

Figure 8. Plotted orbital densities and molecular electrostatic potential (MEP) surfaces at the B3LYP/6-31+g(d,p) level for **4a** and **4b**.

The quantum theory of atoms in a molecule (QTAIM) study reveals the nature of bonding and the surface topology of titled compounds 4a and 4b. The electron density and QTAIM parameters were calculated for (+3; −1), and the bond critical point is also given in Table 6. We have focused more on the interaction pattern and the nature of cationic moiety ($C_5H_{12}N$) with the anionic part in these ionic liquids. The geometries labeled with bond critical points are depicted in Figure 9, while the values are given in Table 6. To attain a better insight into the nature of the hydrogen bond interactions between the dictations and anions of each DIL, the quantum theory of atoms in molecules (QTAIM) can be analyzed. In this theory, the values of electronic density $\rho(r)$ and its Laplacian $\nabla^2\rho(r)$ are used to analyze the topology for classification of bonding interactions in a molecular system. The smaller value of $\rho(r) < 0.1$ au) shows weak van der Waals interactions. For **4a**, the value of $\rho(r)$ is smaller than 0.1 au but has a higher value for the critical point (CP) 136. The above CP (36) corresponds to the interactions between the bonded atoms, which are strongly covalent in nature. Strikingly, all the CP for the interaction of the cationic ring ($C_5H_{12}N$) with molecules are suggesting the non-covalent nature of the bonding. From the laplacian density ($\nabla^2\rho$) and total energy density (H), which is positive, the interactions can be said to be non-covalent for the cationic ring.

Table 6. QTAIM analysis of using BCP (3, −1) for the **4a** and **4b** compound; the values are (in au).

BCP	Interactions	ρ (r)	∇² (r)	G (r)	V (r)	H (r)
4a						
112	O15-O21	0.01242	0.04261	0.00960	−0.00853	0.0010661
111	H49-C23	0.01082	0.03143	0.00681	−0.00576	0.0010481
137	H52-Cl27	0.001360	0.003735	0.0007138	−0.0004936	0.0002201
109	H51-Cl27	0.0021867	0.00616756	0.0011639	−0.0007859	0.00037798
92	H48-O15	0.066432	0.0017422	0.051628	−0.59701	−0.008073
90	H34-O8	0.009801	0.032557	0.0065859	−0.00503255	0.0015534
98	C14-H28	0.0096181	0.0390092	0.0073554	−0.0049584	0.0023969
136	C19-N20	0.46213	0.2099	0.8788	−0.1705	−0.82634
4b						
71	C2-S1	0.20319	−0.382452	0.11288	−0.32139	−0.208505
74	H46-S1	0.042270	0.0500240	0.019821	−0.0271371	−0.0073155
102	H45-S1	0.0512185	0.101639	0.03064215	−0.0358745	−0.0052323
125	O18-C16	0.012298	0.0501636	0.0108061	−0.00907131	0.017348
64	C22-H25	0.0110728	0.044180	0.0085618	−0.00607857	0.00248324
88	H30-H38	0.004022	0.039976	0.0075161	−0.005038	0.00247811

Similarly, for 4b, the CP (71) appeared to be between C2 and S1 and shows a higher value of total electron density $\rho(\mathbf{r})$ as compared to other CPs. Hence, the S-atom has a strong interaction and a covalent nature of bonding with Carbon-2 as indicated by its electron density and negative value of $\nabla^2\rho(r)$. The comparison of QTAIM can be constructed with NBO charges on titled compounds. In **4a**, the negative NBO charges were seen for the nitrogen of $C_5H_{12}N$ ring oxygen atoms in the anionic part. The interaction of H48-atoms of $C_5H_{12}N$-ring with the neighbor O15-atom induces a significant negative charge on it, while hydrogen gets the maximum positive charge. Evidence of a strong interaction can be seen from QTAIM, where $\rho(r)$ was recorded up to 0.066432 au, suggesting strong non-covalent interactions. Likewise, the interaction of other atoms also agreed with the computed NBO charges for the cationic ring and the anionic part. For the 4b, the $C_5H_{12}N$ interacted strongly with the nitrogen and S-atom of the anionic part. The computed negative NBO charges were recorded on nitrogen atoms and sulfur. The charge transfer from the hydrogen H45/H46 of $C_5H_{12}N$-ring to the S-atom may have a strong correlation with the QTAIM study. The significant $\rho(r)$ values are suggesting that a strong non-covalent interaction exists in 4b.

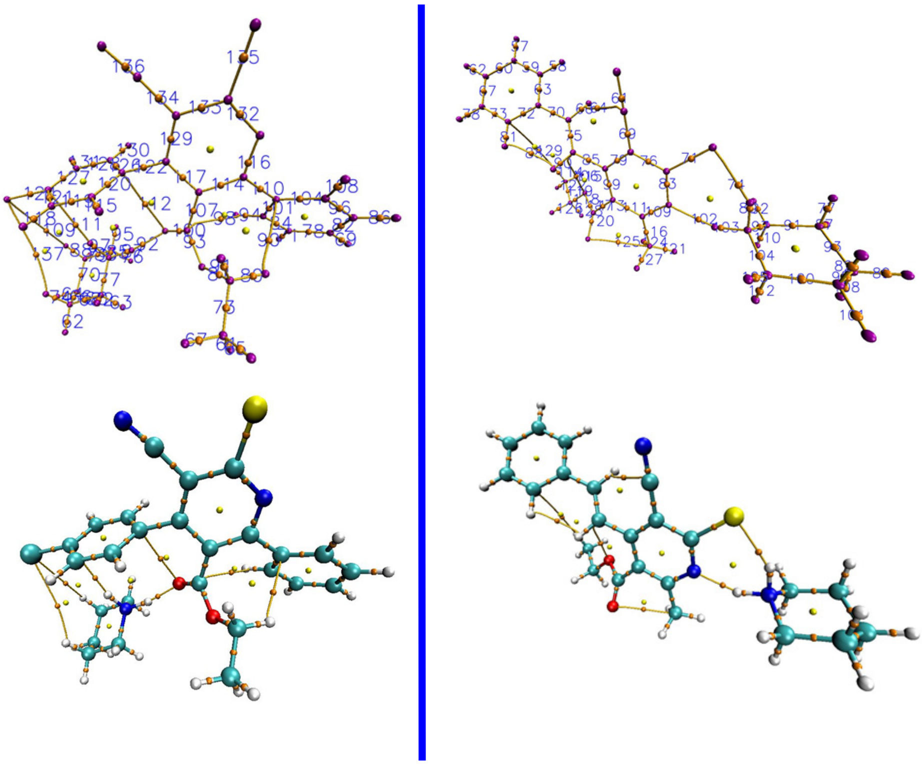

4a

4b

Figure 9. The labeled geometries with bond critical points for **4a** and **4b**.

3.4. *Molecular Electrostatic Potential (MEP)*

The MEP is a helpful computational tool for studying reactivity, because an approaching electrophile will be pulled to negative regions (the electron distribution where the effect is dominant). In the majority of MEPs, the maximum positive region indicating the location for the nucleophilic attack is indicated in blue, whereas the maximum negative region indicating the site for the electrophilic attack is shown in red. The significance of the molecular electrostatic potential (MEP) is that it simultaneously displays the molecular size and shape as well as the positive, negative, and neutral electrostatic potential (MEP) of the compound. The pictorial representations of the MEPs are given in Figure 8. For **4a**, the higher electron density is located around the sulfur and the nitrile nitrogen atoms (red color) of the anion, which favors an incoming electrophile approaching these sites. The region has a low electron density and is located around the cation, which therefore is the region for nucleophilic attack. A similar electron density pattern can be seen for **4b**.

3.5. *Electronic Properties and Global Reactivity of* **4a** *and* **4b**

Chemical reactivity is the study of a molecule's response to an incoming attack by a nucleophile or an electrophile. We estimated the global reactivity descriptors, including ionization potential (IP), electron affinity (EA), chemical hardness (η), chemical potential (μ), and electronegativity (χ), to better understand the reactivity and structural features, using the following equations:

$$\text{Ionization potential (IP)} = -\ \text{E (HOMO)} \tag{1}$$

$$\text{Electron affinity (EA)} = -\text{E (LUMO)} \tag{2}$$

$$\eta = \frac{1}{2}\left(\frac{\partial^2 E}{\partial N^2}\right)\left(\frac{\partial^2 E}{\partial N^2}\right)_{V(r)} = \frac{1}{2}\left(\frac{\partial E}{\partial N}\right)_{V(r)} \tag{3}$$

$$\text{Chemical Hardness } (\eta) = 1/2\ (\text{IP} - \text{EA}) \tag{4}$$

$$\mu = -\chi = \left(\frac{\partial E}{\partial N}\right)_{V(r)} \tag{5}$$

$$\text{Chemical potential } (\mu) = -\frac{\text{IP} + \text{EA}}{2} \tag{6}$$

$$\text{Electronegativity } (\chi) = -\mu \tag{7}$$

$$\text{Electrophilicity index } (\omega) = \mu^2/2\eta \tag{8}$$

The ionization potential and electron affinity were calculated using *Koopmans* approximations in which the negative of the HOMO energy is the IP and the negative of the LUMO energy is the EA. The IP for **4a** is 4.51 eV, while for **4b** it is somewhat larger (5.35 eV, see Table 6), making **4a** electropositive. Similarly, the electron affinities (EA) of **4a** and **4b** are, respectively, 1.72 and 1.95 eV. The higher EA value for **4b** indicates its better electron-accepting tendency as compared to that of **4a**. Chemical systems' behavior toward reactivity and stability can be evaluated using the principle of chemical hardness. It determines how a chemical species offers resistance to change in its electronic configuration. The higher the chemical hardness, the more stable and less reactive the compound (vide supra). The calculated value of η for **4a** is 1.39 eV, while that of **4b** is slightly larger at 1.73 eV. Therefore, **4a** has a softer nature which is more reactive in fragmentation as compared to the nature of **4b**, as shown by the computed HOMO-LUMO gaps. Similarly, the calculated values of electronegativity (χ) for **4a** and **4b** are 3.11 and 3.65 eV, with **4b** being more electronegative than **4a**.

The electrophilicity index (ω) is a gauge of energy loss brought on by the greatest possible electron flow between the donor and acceptor. The calculated ω values describe the biological activity of the compounds and are further used to understand the toxicity of pollutants based on reactivity and site selectivity. The values of ω are 3.47 and 3.89 eV, where **4a** has a slightly smaller value as compared to **4b**. The significant values of the electrophilicity index indicate the strong electrophilic nature of the two compounds.

3.6. Total Density of States (TDOS) Analysis

To understand the electronic and optical properties of **4a** and **4b**, we considered the density of states analysis at the same theoretical level as used earlier, and the spectra are depicted in Figure 10. The TDOS spectra are plotted between the energy range of −21 to 5.44 eV, where the dotted line shows the energy of the highest occupied molecular orbital (HOMO). For **4a**, the new HOMO states appear at high energy, which results in a significant reduction in the HOMO-LUMO gap. Due to the reduced band gap ($E_{\text{H-L}}$), the electron transport becomes easier from HOMO to LUMO, and electrical properties can be triggered. Thus, **4a** has notable electrical properties as compared to **4b**. The higher densities of occupied molecular orbitals and reduced LUMO densities are favorable for classifying **4a** as a good candidate for optical applications.

3.7. Optical and Nonlinear Optical (NLO) Properties

Nonlinear optical (NLO) materials have generated considerable interest due to their widespread applications in data storage devices, optical switching, optical switches, and laser-based endoscopy. Because organic non-linear optical materials are comprised of conjugated molecules, which allow π-electrons to travel freely between the donor and acceptor groups to facilitate charge transfer, they are more efficient by several orders of magnitude and have fast response times as compared to inorganic materials. In compounds, there is a role of non-covalent interaction to structural reactivity and significant charge transfer. In our synthesized ionic liquids, the large dipole moments (μ_o) and asymmetric NBO charge distributions prompted us to further investigate their NLO properties. Nonlinear optical

(NLO) properties are induced by asymmetric charge distribution as well as electronic density that is generated under strong electrical perturbation of light. The energy of the perturbed system is described by the Taylor expansion.

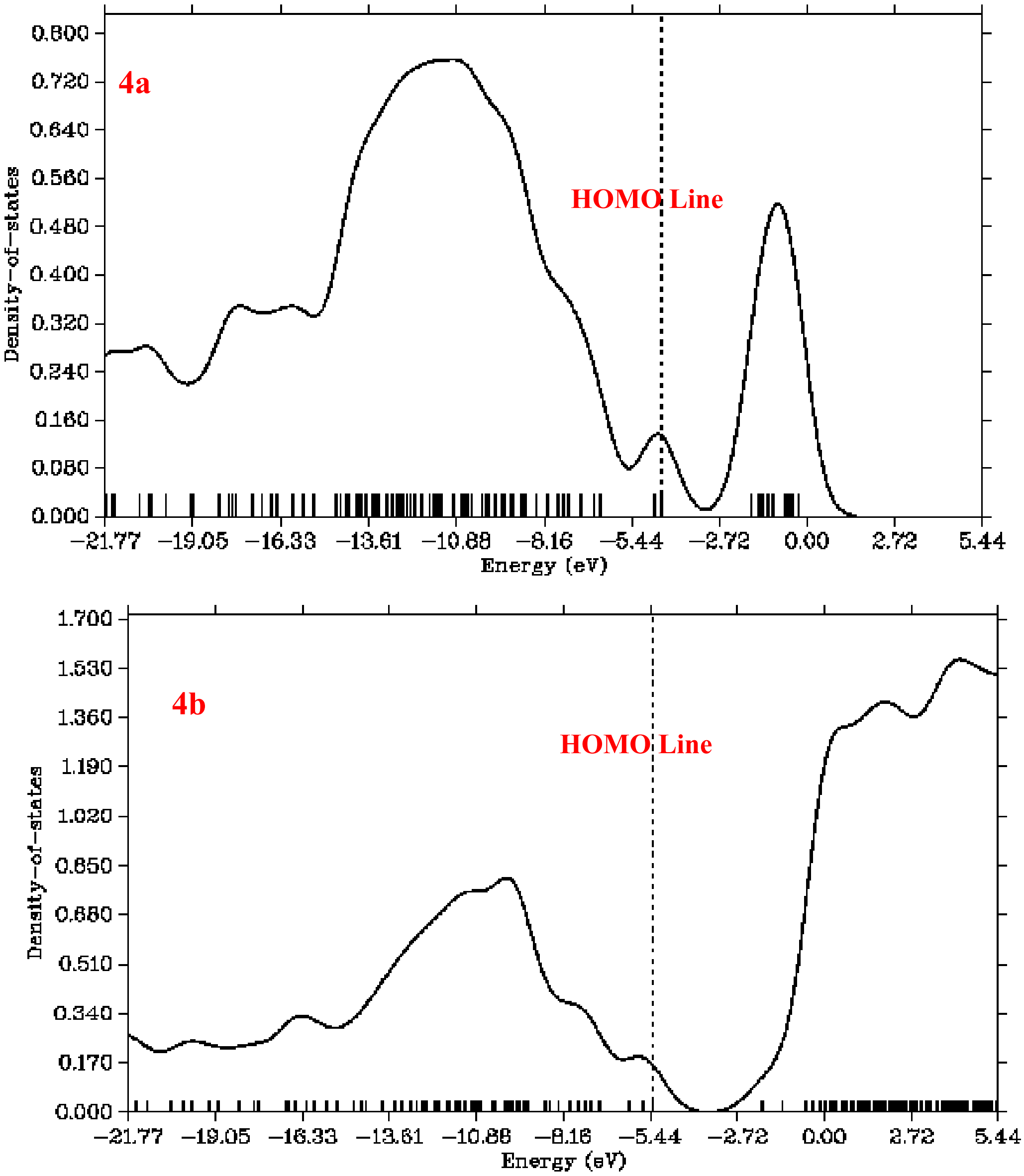

Figure 10. The TDOS spectra of **4a** and **4b**.

$$E = Eo - \mu_I F_i - \left[\frac{1}{2!}\right]\alpha_{ij}F_iF_j - \frac{1}{3!}\beta_{ijk}F_iF_jF_k - \left[\frac{1}{4!}\right]\gamma_{ijkl}F_iF_jF_kF_l \tag{9}$$

E_o is the molecular energy in the absence of the applied electric field; i is the permanent dipole moment along the i direction; F_i is the cartesian component of the applied electric field along the i direction; *ij*, *ijk*, and *ijkl* are the polarizability, first, and second hyperpolarizability tensors, respectively; and i, j, and k are the different components along the x, y, and z directions. The following connection gives the polarizability (α_o) and static hyperpolarizability (β_o):

$$\alpha_o = \frac{1}{3}(\alpha xx + \alpha yy + \alpha zz) \tag{10}$$

$$\beta_o = \sqrt{({\beta^2}_x + {\beta^2}_Y + {\beta^2}_Z)} \tag{11}$$

The computed values of polarizability (α_o), average polarizability volume (α_v), and hyperpolarizability (β_o) are given in Table 4. The obtained values of the polarizabilities for **4a** and **4b** are 402.47 and 368.105 au. The α_o value for **4a** is noticeably larger than that for **4b**, reflecting a larger degree of polarization and asymmetric charge distribution within its structure. The α_o corresponds to the linear response of materials after their interactions with light. The average polarizability volume for **4a** is 59.64 Å^3, while for **4b** it is slightly reduced to 54.54 Å^3. The computed hyperpolarizability for **4a** is 2400.72 au, while for **4b** it is 2722.63 au. Overall, the β_o values for both compounds are noteworthy and are indicate that they are potential candidates for nonlinear optical (NLO) response. The presence of π-conjugation in the anion parts of the compounds might be responsible for triggering NLO values. On the other hand, the presence of non-covalent interactions is also a key factor in boosting the hyperpolarizability values. Hence, the studied ionic liquids are potential candidates for fabricating optoelectronic materials based on their NLO properties.

3.8. Hirschfeld Surface Analysis

CrystalExplorer 17.5 was used for the Hirshfeld surface analysis and the associated two-dimensional fingerprint plots with the experimental atom coordinate as the starting point. The Hirshfeld surfaces of **4a** and **4b** mapped over d_{norm} and d_i are given in Figure 7. A full explanation of these parameters and the interpretation of the plots generated by CrystalExplorer has been published [38]. In **4a**, there are dark red spots adjacent to the C≡N nitrogen and the Cl atoms in the anion, while a fainter red spot appears adjacent to the S atom. An additional dark red spot appears adjacent to an N–H of the cation. These red spots on the d_{norm} surface indicate strong intermolecular interactions, and this is consistent with the intermolecular hydrogen bonding listed in Table 7. Similar comments can be made about the d_{norm} plot for **4b**. The obtained values of the Hirshfeld surface parameters are given in Table 6.

Table 7. The Hirshfeld surface analysis of compounds **4a** and **4b**.

	4a		
	Minimum	**Mean**	**Maximum**
di	0.8622	1.6990	2.7256
de	0.8633	1.6983	2.7694
d_{norm}	−0.3775	0.4886	1.6265
Shapeindex	−0.9972	0.1955	0.9965
curvedness	−4.0821	−0.9298	0.4266
	4b		
	Minimum	**Mean**	**Maximum**
di	0.8219	1.6588	2.6637
de	0.8220	1.6608	2.5890
d_{norm}	−0.4416	0.4854	1.3567
Shapeindex	−0.9991	0.2039	0.9987
curvedness	−3.2614	−0.9192	0.3724

The 2D fingerprint plots (Figure 11) provide information about the types of intermolecular contacts between the atoms and the fractions of their interactions. For the two compounds, the highest van der Waals interaction can be seen between the hydrogen atoms in adjacent fragments and constitute 44.1 and 48% of the total intermolecular interactions for **4a** and **4b**, respectively. The percentage of each internal atom to outside atom contact is given in Table 8. For **4a**, the total volume of the surface is 593.50 Å^3, the area is 489.87 Å^2, the globularity is 0.69, and the asphericity is 0.14. For **4b**, the calculated total volume is 523.90 Å^3, the area is 464.23 Å^2, and the asphericity is 0.676. These values indicate that the compounds deviate from perfect spherical shapes.

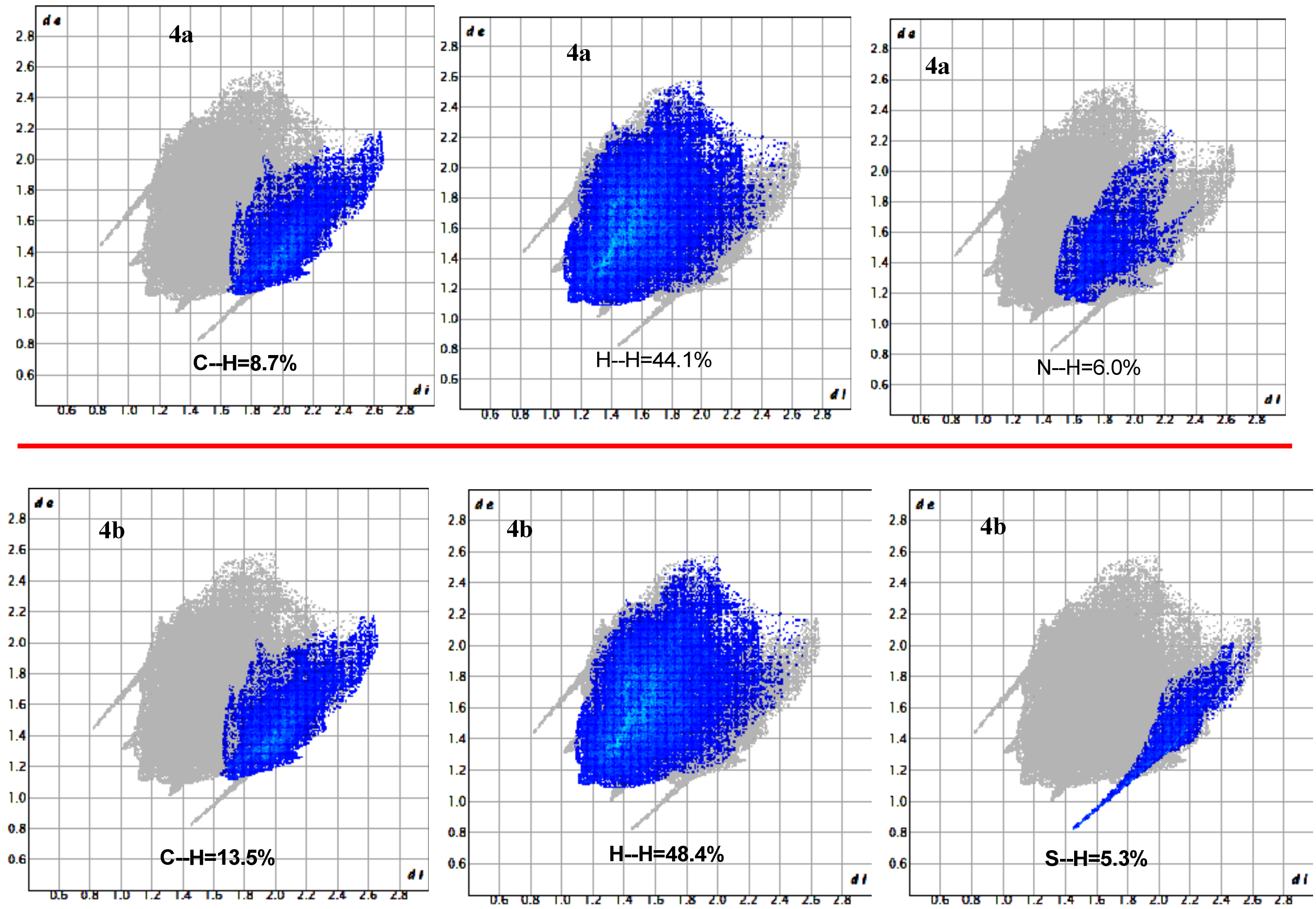

Figure 11. 2D fingerprint plots of **4a** and **4b**.

Table 8. Fingerprints by element type; the surface area included (as a percentage of the total surface area) for close contacts between the atoms inside and outside the surface.

			4a				
Inside Atom				**Outside Atom**			
	Cl	S	O	N	C	H	Total %
C	0.9	-	-	-	0.2	8.7	9.7
Cl	-	-	0.9	0.1	0.8	4.3	6.1
H	2.5	4.5	3.2	5.3	7.4	44.1	67.0
N	0.1	-	-	-	-	6.0	6.1
O	0.7	-	-	-	-	3.4	4.1
S	-	-	-	-	-	6.9	6.9

			4b			
Inside atom			**Outside atom**			
	S	**O**	**N**	**C**	**H**	**Total %**
C	-	0.5	-	0.3	13.5	14.3
H	3.1	2.9	5.2	9.9	48.4	69.6
N	-	0.5	-	-	6.3	6.8
O	-	-	0.5	0.5	3.1	4.0
S	-	-	-	-	5.3	5.3

4. Conclusions

To sum up, we have synthesized two new ionic liquids, and their structures were confirmed using single-crystal X-ray analysis. A DFT investigation using the B3LYP method was carried out to understand the reactivity, optical properties, and nonlinear optical (NLO) properties. The FMO analysis reveals the softer nature of **4a** as compared to **4b** and hence demonstrated its superior reactivity. The HOMO-LUMO gap is 2.78 eV for **4a** and is less than that of **4b**. The NBO study shows the donor properties for the negatively charged oxygen and nitrogen atoms attached to **4a** and **4b**. The global reactivity parameters also indicate their reactivity and optical properties. Nonlinear optical (NLO) properties are indicated by their large polarizability (α_o) and hyperpolarizability (β_o) values. The QTAIM study reveals the role of non-covalent interactions in reactivity between the anionic and cationic fragments. The Hirshfeld surface analysis of the two compounds reveals their intermolecular interactions and reactive sites. The Hirshfeld surfaces and 2D fingerprint plots show important interactions between the anionic fragment and its immediate surroundings. The H···H interactions are much more numerous than those between any other elements in both compounds.

Supplementary Materials: The following supporting information can be downloaded at: https://www.mdpi.com/article/10.3390/cryst13111583/s1. Figure S1: IR spectrum of **4a**; Figure S2: *1*H NMR spectra of **4a**; Figure S3: *13*C NMR spectra of **4a**; Figure S4: IR spectrum of **4b**; Figure S5: *1*H NMR spectra of **4b**; Figure S6: Labeled geometry of compound **4a** and **4b**; Table S1: Total electronic energy (EE), zero-point correction (ZPE), enthalpy, and free energy of **4a** and **4b**; units are in Hartree; Table S2: Optimized coordinated of **4a** and **4b** at the B3LYP/6-31+G(d,p).

Author Contributions: Validation, writing—review and editing, Y.E.B.; Conceptualization and supervision, S.K.M. and E.A.B.; software, analysis, investigation, and resources A.A.; data curation, I.S.M.; writing—original draft preparation, S.A.H.A.-w.; Methodology, J.T.M.; writing and data Curation, and funding acquisition, R.A.-S. All authors have read and agreed to the published version of the manuscript.

Funding: This research was funded by the Researchers Supporting Project No. RSP-2023R353, King Saud University, Riyadh, Saudi Arabia.

Data Availability Statement: No new data were created or analyzed in this study. Data sharing is not applicable to this article.

Acknowledgments: The authors extend their appreciation to the Researchers Supporting Project, King Saud University, Riyadh, Saudi Arabia, for funding this work through grant No. RSP-2023R353.

Conflicts of Interest: The authors declare no conflict of interest.

References

1. Henry, G.D. De novo synthesis of substituted pyridines. *Tetrahedron* **2004**, *29*, 6043–6061. [CrossRef]
2. Vitaku, E.; Smith, D.T.; Njardarson, J.T. Analysis of the structural diversity, substitution patterns, and frequency of nitrogen heterocycles among US FDA approved pharmaceuticals: Miniperspective. *J. Med. Chem.* **2014**, *57*, 10257–10274. [CrossRef] [PubMed]
3. Bakhite, E.A.; Abd-Ella, A.A.; El-Sayed, M.E.A.; Abdel-Raheem, S.A.A. Pyridine derivatives as insecticides. Part 1: Synthesis and toxicity of some pyridine derivatives against Cowpea Aphid, *Aphis craccivora* Koch (Homoptera: Aphididae). *J. Agric. Food Chem.* **2014**, *62*, 9982–9986. [CrossRef] [PubMed]
4. Abbas, I.; Gomha, S.; Elaasser, M.; Bauomi, M. Synthesis and biological evaluation of new pyridines containing imidazole moiety as antimicrobial and anticancer agents. *Turk. J. Chem.* **2015**, *39*, 334–346. [CrossRef]
5. Altaf, A.A.; Shahzad, A.; Gul, Z.; Rasool, N.; Badshah, A.; Lal, B.; Khan, E. A review on the medicinal importance of pyridine derivatives. *J. Drug Des. Med. Chem* **2015**, *1*, 1–11.
6. Shamroukh, A.H.; Kotb, E.R.; Anwar, M.M.; Sharaf, M. A Review on the Chemistry of Nicotinonitriles and Their Applications. *Egypt. J. Chem.* **2021**, *64*, 4509–4529. [CrossRef]
7. He, D.; Wang, B.; Duan, K.; Zhou, Y.; Li, M.; Jiang, H.; Wu, W. Synthesis of Densely Substituted Pyridine Derivatives from 1-Methyl-1, 3-(ar) enynes and Nitriles by a Formal [4 + 2] Cycloaddition Reaction. *Org. Lett.* **2022**, *24*, 1292–1297. [CrossRef]

8. Manna, F.; Chimenti, F.; Bolasco, A.; Filippelli, A.; Palla, A.; Filippelli, W.; Lampa, E.; Mercantini, R. Anti-inflammatory, analgesic and antipyretic 4, 6-disubstituted 3-cyanopyridine-2-ones and 3-cyano-2-aminopyridines. *Eur. J. Med. Chem.* **1992**, *27*, 627–632. [CrossRef]
9. Baldwin, J.J.; Engelhardt, E.L.; Hirschmann, R.; Ponticello, G.S.; Atkinson, J.G.; Wasson, B.K.; Sweet, C.S.; Scriabine, A. Heterocyclic analogs of the antihypertensive. beta.-adrenergic blocking agent (S)-2-[3-(tert-butylamino)-2-hydroxypropoxy]-3-cyanopyridine. *J. Med. Chem.* **1980**, *23*, 65–70. [CrossRef]
10. Alaa, A.-M.; El-Subbagh, H.I.; Kunieda, T. Lewis acid-promoted transformation of 2-alkoxypyridines into 2-aminopyridines and their antibacterial activity. Part 2: Remarkably facile C–N bond formation. *Bioorg. Med. Chem.* **2005**, *13*, 4929–4935.
11. Bekhit, A.A.; Baraka, A.M. Novel milrinone analogs of pyridine-3-carbonitrile derivatives as promising cardiotonic agents. *Eur. J. Med. Chem.* **2005**, *40*, 1405–1413. [CrossRef] [PubMed]
12. El-Sayed, H.A.; Moustafa, A.H.; Haikal, A.E.-F.Z.; Abu-El-Halawa, R.; El Sayed, H. Synthesis, antitumor and antimicrobial activities of 4-(4-chlorophenyl)-3-cyano-2-(β-O-glycosyloxy)-6-(thien-2-yl)-nicotinonitrile. *Eur. J. Med. Chem.* **2011**, *46*, 2948–2954. [CrossRef]
13. Malki, A.; Mohsen, M.; Aziz, H.; Rizk, O.; Shaaban, O.; El-Sayed, M.; Sherif, Z.A.; Ashour, H. New 3-Cyano-2-substituted pyridines induce apoptosis in MCF 7 breast cancer cells. *Molecules* **2016**, *21*, 230. [CrossRef]
14. Abdel-Aziz, H.M.; Gomha, S.M.; El-Sayed, A.A.; Mabkhot, Y.N.; Alsayari, A.; Muhsinah, A. Bin Facile synthesis and antiproliferative activity of new 3-cyanopyridines. *BMC Chem.* **2019**, *13*, 1–10. [CrossRef] [PubMed]
15. Chaubey, A.; Pandeya, S.N. Pyridine a versatile nucleuse in pharmaceutical field. *Asian J. Pharm. Clin. Res* **2011**, *4*, 5–8.
16. Ueda, M.; Matsumura, S.; Masui, M.; Matsuura, E.; Kawakami, M.; Fujitomo, H.; Umeda, T.; Kagawa, H.; Hirohata, S.; Shima, K. Pharmacological studies on a new dihydrothienopyridine calcium antagonist. 3rd communication: Antihypertensive effects of S-(+)-methyl-4, 7-dihydro-3-isobutyl-6-methyl-4-(3-nitrophenyl) thieno [2, 3-b] pyridine-5-carboxylate in hypertensive rats and dogs. *Arzneimittel-forschung* **1993**, *43*, 1282–1290. [PubMed]
17. Al-Trawneh, S.A.; El-Abadelah, M.M.; Zahra, J.A.; Al-Taweel, S.A.; Zani, F.; Incerti, M.; Cavazzoni, A.; Vicini, P. Synthesis and biological evaluation of tetracyclic thienopyridones as antibacterial and antitumor agents. *Bioorg. Med. Chem.* **2011**, *19*, 2541–2548. [CrossRef]
18. Madhusudana, K.; Shireesha, B.; Naidu, V.G.M.; Ramakrishna, S.; Narsaiah, B.; Rao, A.R.; Diwan, P. V Anti-inflammatory potential of thienopyridines as possible alternative to NSAIDs. *Eur. J. Pharmacol.* **2012**, *678*, 48–54. [CrossRef]
19. Bousquet, E.; Guerrera, F.; Siracusa, M.A.; Caruso, A.; Amico-Roxas, M. Synthesis and pharmacological activity of 3-substituted pyrido [3′, 2′: 4, 5] thieno [3, 2-d] pyrimidin-4 (3H)-ones. *Farmaco. Sci.* **1984**, *39*, 110–119. [CrossRef]
20. Bousquet, E.; Romeo, G.; Guerrera, F.; Caruso, A.; Amico-Roxas, M. [Synthesis and analgesic activity of 3-substituted derivatives of pyrido [3′, 2′: 4, 5] thieno [3, 2-d] pyrimidin-4 (3H)-ones]. *Farmaco. Sci.* **1985**, *40*, 869–874.
21. Hussein, A.M.; Abu-Shanab, F.A.; Ishak, E.A. The multi-component condensation in the synthesis of the substituted 2-alkylsulphanil-4, 6-diarilpyridine-3-carbonitriles and their derivatives. *Phosphorus Sulfur. Silicon. Relat. Elem.* **2000**, *159*, 55–68. [CrossRef]
22. Quintela, J.M.; Peinador, C.; Veiga, C.; González, L.; Botana, L.M.; Alfonso, A.; Riguera, R. Synthesis and antiallergic activity of pyridothienopyrimidines. *Bioorg. Med. Chem.* **1998**, *6*, 1911–1925. [CrossRef] [PubMed]
23. Madding, G.D.; Thompson, M.D. Regioselective syntheses of 2-amino-4, 5-dialkylthiophene-3-carboxylates and their conversion to 3, 4-dihydro-4-oxothieno [2, 3-d] pyrimidine-2-carboxylates. *J. Heterocycl. Chem.* **1987**, *24*, 581–587. [CrossRef]
24. Böhm, N.; Krasselt, U.; Leistner, S.; Wagner, G. Reactions of 4-oxo-4H-pyrido (3′, 2′: 4, 5) thieno (3, 2-d)-1, 3-oxazines with amines. *Pharmazie* **1992**, *47*, 897–901.
25. Wagner, G.; Leistner, S.; Vieweg, H.; Krasselt, U.; Prantz, J. Synthesis of thieno (2, 3-b) pyridines with oxalamidic acid or an oxalamidic alkylester residues and of 4-alkoxy-pyrido (3′, 2′: 4, 5) thieno (3, 2-d) pyridine-2-carboxylic acid derivates. *Pharmazie* **1993**, *48*, 342–346.
26. Dai, X.-Y.; Zeng, X.-X.; Peng, F.; Han, Y.-Y.; Lin, H.-J.; Xu, Y.-Z.; Zhou, T.; Xie, G.; Deng, Y.; Mao, Y.-Q. A novel anticancer agent, SKLB70359, inhibits human hepatic carcinoma cells proliferation via G0/G1 cell cycle arrest and apoptosis induction. *Cell. Physiol. Biochem.* **2012**, *29*, 281–290. [CrossRef]
27. Lockman, J.W.; Reeder, M.D.; Suzuki, K.; Ostanin, K.; Hoff, R.; Bhoite, L.; Austin, H.; Baichwal, V.; Willardsen, J.A. Inhibition of eEF2-K by thieno [2, 3-b] pyridine analogues. *Bioorg. Med. Chem. Lett.* **2010**, *20*, 2283–2286. [CrossRef]
28. Wu, J.-P.; Fleck, R.; Brickwood, J.; Capolino, A.; Catron, K.; Chen, Z.; Cywin, C.; Emeigh, J.; Foerst, M.; Ginn, J. The discovery of thienopyridine analogues as potent IκB kinase β inhibitors. Part II. *Bioorg. Med. Chem. Lett.* **2009**, *19*, 5547–5551. [CrossRef]
29. Egorova, K.S.; Gordeev, E.G.; Ananikov, V.P. Biological Activity of Ionic Liquids and Their Application in Pharmaceutics and Medicine. *Chem.Rev.* **2017**, *117*, 7132–7189. [CrossRef]
30. Singh, S.K. Solubility of lignin and chitin in ionic liquids and their biomedical applications. *Int. J. Biol. Macromol.* **2019**, *132*, 265–277. [CrossRef]
31. Singh, S.K.; Savoy, A.W. Ionic liquids Synthesis and applications: An overview. *J. Mol. Liq.* **2020**, *297*, 112038–112060. [CrossRef]
32. Welton, T. Room-temperature ionic liquids. Solvents for synthesis and catalysis. *Chem. Rev.* **1999**, *99*, 2071–2084. [CrossRef] [PubMed]
33. Hallett, P.; Welton, T. Room-temperature ionic liquids: Solvents for synthesis and catalysis. 2. *Chem. Rev.* **2011**, *111*, 3508–3576. [CrossRef] [PubMed]

34. Fox, D.M.; Awad, W.H.; Gilman, J.W.; Maupin, P.H.; De Long, H.C.; Trulove, P.C. Flammability, thermal stability, and phase change characteristics of several trialkylimidazolium salts. *Green Chem.* **2003**, *5*, 724–727. [CrossRef]
35. Zang, H.; Feng, Y.; Lou, J.; Wang, K.; Wu, C.; Liu, Z.; Zhu, X. Synthesis and performance of piperidinium-based ionic liquids as catalyst for biomass conversion into 3-acetamido-5-acetylfuran. *J. Mol. Liq.* **2022**, *366*, 120281. [CrossRef]
36. Bruker. *APEX3, SAINT and SADABS*; Bruker AXS Inc.: Madison, WI, USA, 2016; p. 2014.
37. Sheldrick, G.M. SHELXT—Integrated space-group and crystal-structure determination. *Acta Crystallogr. Sect. A Found. Crystallogr.* **2015**, *71*, 3–8. [CrossRef]
38. Sheldrick, G.M. Crystal structure refinement with SHELXL. *Acta Crystallogr. Sect. C Struct. Chem.* **2015**, *71*, 3–8. [CrossRef]
39. Ahsin, A.; Ayub, K. Superalkali-based alkalides Li3O@[12-crown-4]M (where M = Li, Na, and K) with remarkable static and dynamic NLO properties; A DFT study. *Mater. Sci. Semicond. Process.* **2022**, *138*, 106254. [CrossRef]
40. Caricato, M.; Frisch, M.J.; Hiscocks, J.; Frisch, M.J. *Gaussian 09: IOps Reference*; Gaussian Inc.: Wallingford, CT, USA, 2009; ISBN 0972718788.
41. Dennington, R.; Keith, T.; Millam, J. *GaussView*; Version 5; Semichem Inc.: Shawnee, KS, USA, 2009.
42. Tirado-Rives, J.; Jorgensen, W.L. Performance of B3LYP density functional methods for a large set of organic molecules. *J. Chem. Theory Comput.* **2008**, *4*, 297–306. [CrossRef]
43. Spackman, P.R.; Turner, M.J.; McKinnon, J.J.; Wolff, S.K.; Grimwood, D.J.; Jayatilaka, D.; Spackman, M.A. CrystalExplorer: A program for Hirshfeld surface analysis, visualization and quantitative analysis of molecular crystals. *J. Appl. Crystallogr.* **2021**, *54*, 1006–1011. [CrossRef]